Lawrence Berkeley National Laboratory
LBL Publications

Title
X-ray ptychography on low-dimensional hard-condensed matter materials

Permalink
https://escholarship.org/uc/item/5vt5p4vv

Journal
Applied Physics Reviews, 6(1)

ISSN
1931-9401

Authors
Shi, Xiaowen
Burdet, Nicolas
Chen, Bo
et al.

Publication Date
2019-03-01

DOI
10.1063/1.5045131

Peer reviewed

X-ray ptychography on low-dimensional hard-condensed matter materials

Xiaowen Shi, Nicolas Burdet, Bo Chen, Gang Xiong, Robert Streubel (iD), Ross Harder, and Ian K. Robinson
(iD)

View Online   Export Citation   CrossMark

ARTICLES YOU MAY BE INTERESTED IN

Journal
Impact Factor
12.750

Applied Physics Reviews
Submit your original research **today!**   LEARN MORE >>>

X-ray ptychography on low-dimensional hard-condensed matter materials

View Online   Export Citation   CrossMark

Xiaowen Shi,[1,a),b)] Nicolas Burdet,[2,b)] Bo Chen,[3,4] Gang Xiong,[5] Robert Streubel,[6] [iD] Ross Harder,[7]
and Ian K. Robinson[4,8] [iD]

AFFILIATIONS

[1]Diamond Light Source Ltd., Harwell Science and Innovation Campus, Didcot, Oxfordshire OX11 0DE, United Kingdom
[2]Advanced Light Source, Lawrence Berkeley National Laboratory, Berkeley, California 94720, USA
[3]School of Materials Science and Engineering, TongJi University, Shanghai 201804, China
[4]London Centre for Nanotechnology, University College London, London WC1H 0AH, United Kingdom
[5]Department of Chemistry, University of Cambridge, Cambridge CB2 1EW, United Kingdom
[6]Materials Sciences Division, Lawrence Berkeley National Laboratory, Berkeley, California 94720, USA
[7]Advanced Photon Source, Argonne, Illinois 60439, USA
[8]Department of Condensed Matter Physics and Materials Science, Brookhaven National Laboratory, Upton, New York 11973, USA

a)Electronic addresses: xiaowen.shi@diamond.ac.uk and xiaowen.shi@cantab.net. **Telephone:** +44 (01235) 567509.
b)**Contributions:** X. Shi and N. Burdet contributed equally to this work.

ABSTRACT

Tailoring structural, chemical, and electronic (dis-)order in heterogeneous media is one of the transformative opportunities to enable new functionalities and sciences in energy and quantum materials. This endeavor requires elemental, chemical, and magnetic sensitivities at the nano/atomic scale in two- and three-dimensional space. Soft X-ray radiation and hard X-ray radiation provided by synchrotron facilities have emerged as standard characterization probes owing to their inherent element-specificity and high intensity. One of the most promising methods in view of sensitivity and spatial resolution is coherent diffraction imaging, namely, X-ray ptychography, which is envisioned to take on the dominance of electron imaging techniques offering with atomic resolution in the age of diffraction limited light sources. In this review, we discuss the current research examples of far-field diffraction-based X-ray ptychography on two-dimensional and three-dimensional semiconductors, ferroelectrics, and ferromagnets and their blooming future as a mainstream tool for materials sciences.

TABLE OF CONTENTS

I. INTRODUCTION

Low-dimensional materials are systems with at least one spatial dimension limited to a maximum of 100 nm. These structures are typically referred to as zero-, one-, or two-dimensional depending on their spatial confinement and can exhibit distinct properties due to confinement and energy quantization in correlated electron systems and quantum materials. The common examples of low-dimensional solid-state materials include transition metals, half metals, rare-earth elements, and the corresponding oxide compounds, functioning as semiconductors, superconductors, batteries, ferroelectrics, ferromagnets, and multiferroics. Understanding the role of structural, chemical, and electronic (dis-)order in the properties of these complex,

heterogeneous systems is the foundation for engineering next-generation nano-scale quantum materials with tailored functionality for, e.g., novel electronics. Thus far, imaging techniques relying on electrons and X-rays have significantly contributed to the advancement of synthesis science, materials optimization, and device operation. While electron microscopy, tomography, and diffraction with aberration correction and advanced reconstruction algorithms have dominated structural characterization owing to a spatial resolution down to single atoms, synchrotron X-ray radiation has emerged as a standard for chemical and magnetic characterization benefiting from an inherent element-specificity and high intensity. One of the most promising methods in view of sensitivity and spatial resolution is coherent diffraction imaging, namely, X-ray ptychography,[1] which is envisioned to take on the dominance of electron imaging techniques in the rising age of diffraction limited light sources. Advances in reconstruction algorithms, beam lines, and end stations, as well as the prospect of fully coherent beams with next-generation light sources, have fueled appeal and enthusiasm of researchers worldwide to adapt X-ray ptychography for their science taking advantage of high-resolution phase-contrast imaging. In particular, the current world-record in spatial resolution for soft and hard X-ray ptychography is 5 nm[2] and <15 nm,[3] respectively. The technique itself can be divided as follows: forward geometry: transmission ptychography,[2] multi-slicing ptychography,[4–6] although the technique is currently at its infancy, and ptychographic X-ray computed tomography (PXCT)[7] and Bragg geometry: Bragg projection ptychography (BPP) and 3D Bragg ptychography. PXCT relies on the tomographic reconstructions of at least one series of 2D ptychographic projections, where tomographic reconstructions could be carried out on a series of 2D ptychographic projections using back-projection algorithms or other advanced algorithms.[8] It offers a spatial resolution down to 16 nm[9] and 14.6 nm[10] in 3D in hard X-rays and 11 nm[11] in 3D soft X-rays.

II. PTYCHOGRAPHY: A SCANNING COHERENT X-RAY DIFFRACTION IMAGING (CXDI) METHOD

A. Overview and introduction

Developments in semiconductor and spin-based nano-electronical devices during the past few decades have been driving scientists and engineers to invent advanced imaging methods to provide solutions for the characterization of next-generation nano-devices. The ability to fabricate ultra-miniaturized nano-devices on an industrialized scale for commercialization demands that these devices are characterized with suitably high-resolution imaging tools. The current high-resolution imaging techniques allow researchers to access the fundamental length scale in nano-scale device technologies, previously inaccessible due to the lack of available imaging tools. The fundamental length scale is typically on the order of a few nanometers to tens of nanometers, where quantum mechanical phenomena in systems under study become relevant. As a result, this has opened a new field of research that focuses on the study of nano-scale phenomena in low-dimensional structures. Electron-based imaging techniques such as high-resolution transmission electron microscopy (HRTEM) and photoemission electron microscopy (PEEM) mechanisms are widely used for the characterization of nanostructure dynamics.[12,13] Transmission X-ray Microscopy (TXM) and Scanning Transmission X-ray Microscopy (STXM), especially in the soft

X-ray regime, are regularly used for high-resolution real-space imaging for magnetic systems.

For imaging techniques that involve reciprocal-space that is the corresponding Fourier transform of the real-space wave function, X-ray holography is a technique that employs the coherence of X-rays to produce constructive and destructive interferences between the exit sample wavefunction and the reference wavefunction. As a result, the retrieval of structural information that is encoded in phase components of sample complex wavefunctions is accomplished. The technique was first experimentally demonstrated by Eisebitt et al.[14] and applied to magnetic thin film domain systems.[15]

Another reciprocal-space imaging technique that was invented about two decades ago is coherent X-ray diffraction imaging (CXDI). CXDI[16] is the very first lensless diffraction imaging technique, which is widely used in materials science applications. This technique is used to study biological samples,[17–19] single crystalline materials,[20] and other condensed matter samples. CXDI in reflection geometry has also been demonstrated.[21] The fundamental principle behind CXDI is the use of advanced iterative algorithms to reconstruct the real-space complex sample wavefunction through reciprocal-space coherent diffraction intensities with a stringent oversampling criterion.[22] CXDI data reconstructions sometimes can result in non-unique inversion solutions, and the elegant amalgamation of scanning transmission X-ray microscopy (STXM) with CXDI, namely ptychography, has the potential to address this fundamental problem that poses an obstacle in CXDI. The rapid development of ptychography in the recent decade has significantly improved the data reconstruction efficiencies and should effectively alleviate the non-uniqueness solution problems in CXDI.[23] Researchers also combined holography with CXDI in the reflection geometry[24] and applied holography in conjunction with ptychography as recently reported.[25] Sections II B and II C provide discussions on forward and Bragg geometry ptychography methods for nanoscale materials science characterization studies.

B. Forward geometry ptychography

Ptychography is a technique that was originally invented by Hoppe[26] in the 1960s. Initially, the technique was proposed to study the phase problem by recording overlapping Bragg reflections in electron diffraction experiments using a convergent beam. After a decade of development of coherent X-ray diffraction imaging (CXDI)[16,20,27] methods, Rodenburg et al.[28] combined both STXM and CXDI to study the extended samples, which became ptychography in modern age. The "overlap constraint"[28,29] is moved to real-space, and it is used in ptychography iterative algorithms as illustrated in the diagram in Fig. 1. The details of mathematical and experimental concepts of X-ray coherence along with how overlap and modulus constraints work in ptychography are extensively discussed in Ref. 30 and Refs. 28, 29, and 31, respectively. The initial iterative algorithms used in ptychography are categorized as ptychographic iterative engine (PIE)[28] and extended-PIE.[32] In the PIE algorithms, the concepts are easy to grasp as the real-space update proceeds in a serial fashion. The PIE algorithms work well when the probe is not fluctuating or unstable. Another type of ptychographic algorithm incorporates the original difference-map method[29,33] to decipher object and probe being updated in parallel. As a result, the algorithms are more rigorous mathematically, and the data inversion convergence can be reached more aggressively. The relaxed averaged alternating reflection
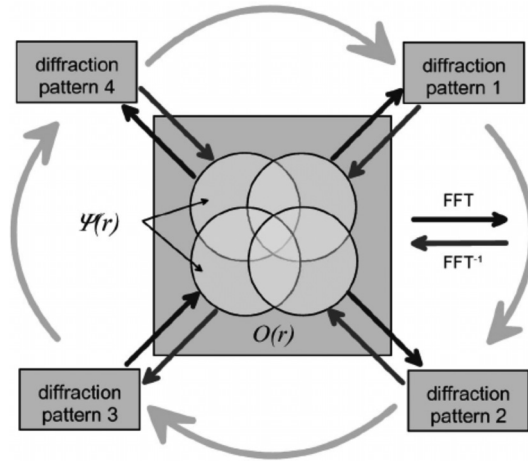
FIG. 1. Illustration of the earliest ptychographic iterative engine. The update of the object and probe function is in a sequential order. Reprinted with permission from Rodenburg et al., Phys. Rev. Lett. **98**(3), 034801 (2007). Copyright 2007 American Physical Society.

(RAAR)[2,34,35] algorithms have more advanced real-space overlap constraint compared to that of the difference map; therefore, in principle, it maximizes the rate of data reconstruction convergence. Data redundancies in ptychography allow for the algorithms to take into account the experimental imperfections such as fluctuating diffraction intensities, background noises, and position imprecisions. As an example, the maximum-likelihood is an extension on the original PIE[36] and difference-map,[37,38] which incorporates the character of Gaussian or Poisson photon counting and the associated photon noises in real experiments into the ptychographic iterative algorithms to optimize data inversion quality. Furthermore, a class of very refined algorithms termed augmented projection ptychographic algorithms account for fluctuating intensities, position errors, poor calibration using multiplexing illumination, and unknown background offset[39] in experimental data. The method is promising for high-quality ptychographic reconstructions of experimental data with undesirably low-counting statistics and imperfections in the data acquisitions. Ptychographic algorithms using partially coherent X-rays[40–43] increase the data reconstruction efficiency and coherent flux on sample. The utilization of fly-scan ptychography[44,45] elegantly enables fast sample stage scans with continuous motion, and it could significantly improve ptychographic data collection efficiency and speed. Partial coherence in the transverse direction is usually originated from synchrotron beamline instabilities, such as vibrations of X-ray upstream general optics, double-crystal monochromators, or X-ray focusing optics. The introduction of a relatively large band-width monochromator such as multi-layer monochromator (MLM) might result in a relatively lower longitudinal coherence length. In some cases, transverse partial coherence can originate from sample stage vibrations or instabilities of the sample itself, introducing multiple modes in the complex object wavefunction. Multi-modal considerations into ptychographic algorithms are discussed at the end of Sec. II B "Forward geometry ptychography." Moreover, the rapid developments of real-time ptychography data reconstruction software packages in multiple synchrotron facilities such as Advanced Photon Source (APS),[46] SHARP

(scalable heterogeneous adaptive real-time ptychography) at Advanced Light Source,[35,47] and National Synchrotron Light Source II (NSLS II)[48] deliver simultaneous ptychographic data collection and inversion with a speed on the order of up to a few seconds at some beamlines.

Ptychography was developed primarily for the study of extended specimens, whereas the initial CXDI technique was introduced to solve the "phase problem" inherent to diffraction.[49–51] The most notable issue of the "phase problem" is the fact that the phase information in the exit wavefunction is lost during measurements. This is because the diffraction intensities recorded on a detector are the modulus squared of the exit wavefunction. As a result, the direct retrieval of structural information that is encoded in the phase component of the complex sample wavefunction is not possible. By applying advanced iterative algorithms in ptychography, complex wavefunctions of both the sample and probe can be indirectly recovered. Ptychography can be performed with just a simple pinhole to select the appropriate coherence level in experiments, such as that performed in the very first ptychography measurements.[7,29]

In forward geometry, the sample, X-ray optics, and X-ray detectors are co-linear, and depending on the Fresnel numbers, there are two classifications of forward geometry: near-field[52] and far field ptychography.[28] The near-field (Fresnel) or far-field (Fraunhofer) illumination of X-rays in ptychography experimental setups is based on the diffracted wave-front curvature and the associated angular distribution on the detector. In the near-field regime, the interferences of the exit waves after the sample are of high curvature due to the relatively short sample-detector distance. Here, we define that the near-field region is where sample-detector distance $D < a^2/\lambda$, where a^2 is the X-ray illuminated area and λ is the wavelength of the incident X-rays. On the other hand, when $D > a^2/\lambda$, the curvature of the diffracted wave-fronts becomes less pronounced. A further increase in D does not change the angular distribution of the experimental diffraction patterns in the far-field regime.[53]

In this review, only far-field diffraction based ptychography techniques are discussed. Forward-geometry ptychography in the far-field region collects coherent diffraction intensities, similar to the experimental geometry of small-angle X-ray scattering (SAXS)[54] or wide-angle X-ray scattering (WAXS).[55] X-ray focusing optics is typically used in ptychography measurements when high flux is required for weak-scattering samples. When using focusing optics, the resulting X-ray probes have complicated structures due to the nature of the focusing mechanisms. The fringes of probes at the focusing spots are generally sinc function-like from Kirkpatrick-Baez (KB) mirrors[56,57] and Airy disk-like from Fresnel Zone Plates (FZPs).[2,11,58,59] A coherence-defining-aperture (CDA) is typically used to define the incoming X-rays within the acceptable lateral coherence length to achieve the coherence level in the transverse directions (both in the horizontal and vertical directions), and it is usually located upstream of the focusing optics. In the typical 3rd generation synchrotron radiation beamlines, the size of CDA is usually chosen to be of one lateral coherence length.[60] The sinc function-like fringes in the focusing probe from the KB mirrors are usually originated from the CDA, which is usually a square slit.

Figure 2 shows a typical ptychography experimental setup[2] using a FZP as a focusing optics at the Advanced Light Source, Lawrence Berkeley National Laboratory.
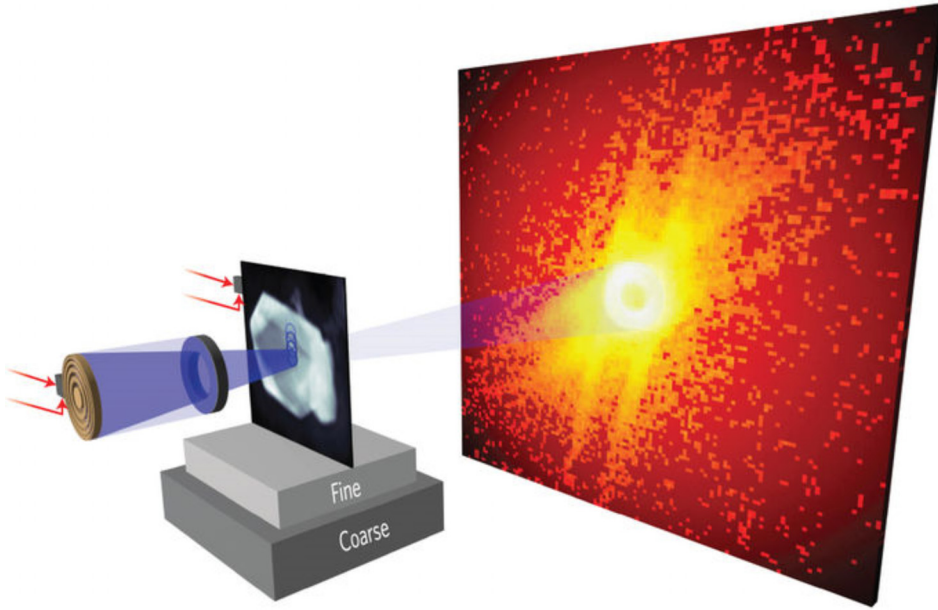
FIG. 2. Layout of the soft X-ray ptychographic microscope. "Fine" and "Coarse" in this image illustrate the high-resolution "Fine" piezo-stage and the low-resolution "Coarse" counterpart used in the ptychographic imaging setups. The red arrows show the interferometers that measure relative displacements between the Fresnel Zone Plate and the sample stage in the scanning directions with 1.5 nm resolution. The blue and brown components show the Fresnel Zone Plate and the Order Sorting Aperture in the experimental setup, respectively. Reprinted with permission from Shapiro *et al.*, Nat. Photonics **8**(10), 765–769 (2014). Copyright 2014 Macmillan Publishers Ltd.

To collect ptychography datasets, X-ray beam illuminating areas are made to overlap between the adjacent scan positions, typically by 50%–85%. X-ray probe sizes on the sample can be from 50 nm to tens of microns, which are carefully selected by considering the experimental setup stability and the field-of-view required for the interesting regions of the samples.

Coherent diffraction patterns are then collected at each scan position by high performance X-ray detectors, with most hard X-ray beamlines currently using photon-counting area detectors, while charge-coupled device (CCD) detectors are commonly used in soft X-ray beamlines. Coherent diffraction patterns are reconstructed by the ptychographic iterative algorithms to image both the complex probe wave functions and the real-space complex objects. Ptychography with the upsampled data[61,62] has been successful by trading off oversampling for overlap. The upsampling technique utilizes the excessive overlap ratio in real-space to compensate overall sampling conditions for deficiencies in reciprocal-space oversampling ratios. Some important findings show that the introduction of a diffuser in hard X-ray ptychography has led to improved ptychographic reconstructions on strongly patterned samples.[63,64] The introduction of a diffuser strengthens the diversity of the X-ray probe structures, which could, in principle, aid ptychographic data convergence but may require prior knowledge of the diffuser structure.

The reciprocal-space coherent diffraction intensities can be expressed as follows:

$$I_j(q) = |FT[p(r - r_j)^* o(r)]|^2 = |FT[\psi_j(r)]|^2, \quad (1)$$

where FT denotes the Fourier Transform operation, $p(r - r_j)$ is the complex probe function, and $o(r)$ corresponds to the complex object function in real-space. "*" denotes the multiplication operation, and $\psi_j(r)$ is the real-space complex overall function, which is the product of the probe and the object complex functions. The reciprocal-space complex wave function can be written as

$$\Psi'_j(q) = \sqrt{I_j} \cdot \exp\left(i\hat{\phi}_j\right), \quad (2)$$

where $\hat{\phi}_j$ denotes the phase part of the wave function intensity I_j at the detector pixel position j and $\Psi'(q)$ is the updated exit wave function

$$\psi'_j(r) = FT^{-1}\left[\Psi'_j(q)\right], \quad (3)$$

where FT^{-1} denotes the inverse Fourier Transform operation and $\psi'_j(r)$ is the updated real-space wave function. Equations (1)–(3) represent the Fourier-space modulus constraint operation, which is usually condensed into the operator Π_F.

In PIE algorithms, the real-space object update function, which is also the real-space overlap constraint operation, thus can be expressed as follows:

$$o_j^{n+1}(r) = o_j^n(r) + \frac{|p(r + r_j)| p^*(r + r_j)}{|p_{max}(r + r_j)||p(r + r_j)|^2 + \alpha} \cdot \beta\left(\psi'_j(r) - \psi_j(r)\right), \quad (4)$$

where $o_j^{n+1}(r)$ is the updated complex object function from the previous complex object function $o_j^n(r)$. α is a term used to avoid numerical problems when the complex probe function $p(r + r_j)$ is approximately equal to 0, and β is a feedback parameter that is typically chosen to be between 0.5 and 1. Equation (4) can be interpreted as the real-space overlap constraint operation Π_0 in the PIE algorithms.

In the difference-map ptychographic algorithms, the real-space overlap constraint Π_0 manifests to be the updates of both the object and the probe complex functions as follows:

$$o_{new}(r) = \frac{\sum_j p^*(r + r_j) \cdot \psi_j(r)}{\sum_j |p(r + r_j)|^2}, \quad (5)$$

$$p_{new}(r) = \frac{\sum_j o^*(r - r_j) \cdot \psi_j(r)}{\sum_j |o(r - r_j)|^2}, \quad (6)$$

where the overall real-space overlap constraint update procedure can be expressed as follows:

$$\psi_{n+1} = \psi_n + \Pi_F \left(2\Pi_0 \left(\psi_n \right) - \psi_n \right) - \Pi_0 \left(\psi_n \right), \qquad (7)$$

where Π_F is the Fourier-space modulus constraint operation, which is equivalent to Eqs. (1)–(3). Π_0 is the real-space overlap constraint operation, which is equivalent to Eq. (4).

When partial coherence is introduced into the ptychographic algorithms, multiple modes of both the sample and the probe need to be considered and incorporated into the ptychographic iterative algorithms. This topic has been extensively discussed in a recent review paper,[65] and the principles have also been described in many recent publications.[40–43]

C. Bragg ptychography

Ptychography in Bragg geometry has promised potential applications in compact or extended single crystalline nano-structures, with its special emphasis on surface sciences and thin film specimens. Three-dimensional atomic displacement fields inside a single crystal object can then be reconstructed.

This technique is an extension of a previously well-known method, Bragg Coherent diffraction imaging (Bragg CDI).[20,27] Studies on isolated single crystalline structures by Bragg CDI have been investigated by the current state-of-art instrumentations at available beamline worldwide, such as 34-ID-C at the Advanced Photon Source (APS), ID-01 and ID-13 at the European Synchrotron Radiation Facilities (ESRF), and I13 at the Diamond Light Source (DLS). To advance this technique further, Bragg-geometry ptychography is considered advantageous over the conventional Bragg CDI because of the overlapping of scan positions being introduced into the coherent diffraction intensities in two- or three-dimensional datasets. If the experimental setups are sufficiently stable, the arbitrarily large field-of-view can be measured for extended samples. One constraint for Bragg ptychography is that probe structures have to be known *a priori* as the

technique currently does not allow simultaneous reconstructions of both the sample and the probe.

Bragg-geometry ptychography is thought to be much more robust for solving highly strained structures because of the inherent nature of overlap in real-space during data acquisition and algorithms. These problems still remain difficult in the conventional Bragg CDI although many attempts have shown solutions to overcome the problems in some recent studies.[66–70]

One of the major challenges to the successful data inversion of the Bragg ptychography in reflection-geometry is to make sure that the optical path length difference (OPLD) is always equal to or smaller than the longitudinal coherence length of a particular experimental setup.[71] It is thus important to properly estimate the OPLD throughout the measurements in Bragg-reflection geometry ptychography.

Figure 3 shows the Bragg projection ptychography (BPP) ray diagram[72] by performing beam scanning in the laboratory frame; the beam displacement that follows the projected overlap is considered symmetric with equal step-sizes within the experimental detector plane (a'b' = −a''b'') for the specular diffraction geometry. The specular diffraction geometry of BPP is shown in Fig. 3, and it is demonstrated nicely on the diffraction symmetry in the specular case where the sample of interest is a thin film single crystalline system. Due to the reflection geometry of the BPP, only sample information in the projected slice is fully inverted in the iterative reconstructions. Bragg ptychography in Laue geometry has also been demonstrated with co-linear diffraction geometry on biological matters.[73,74]

BPP was developed on the 2D projection approach and demonstrated by Hruszkewycz *et al.*[75–78] BPP uses the data collected through two-dimensional projections at the Bragg condition when the diffraction intensities are the highest rather than three-dimensional Bragg peaks collected as in Bragg CDI. A recent study carried out detailed analysis on the feasibilities of studying thin film domain structures by BPP.[75] In general, the 2D approach is justified by the Fourier slice theorem: a 2D planar cross section of the 3D intensity pattern in reciprocal space (e.g., at a Bragg peak) is the Fourier transform of the projection in real space. The detailed concepts of the Fourier slice
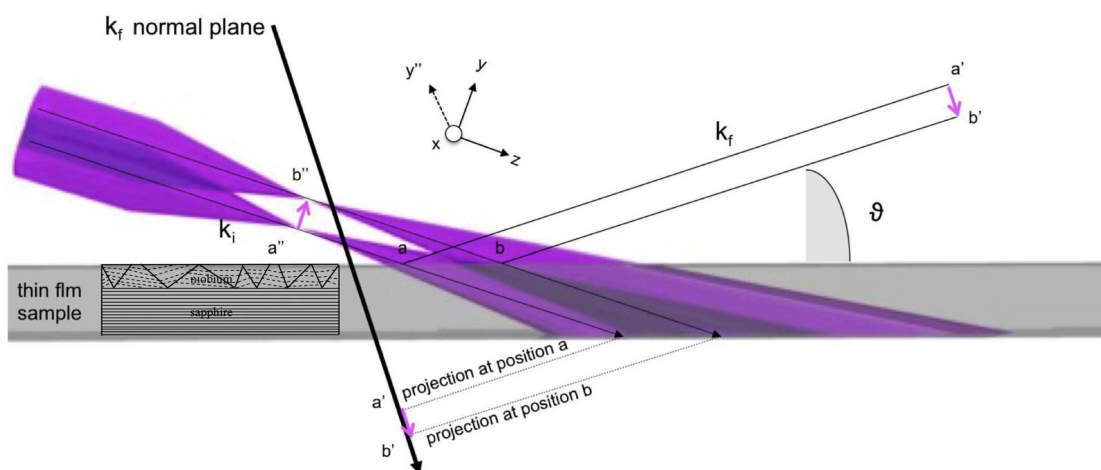

FIG. 3. Schematic of Bragg projection on an idealized niobium thin film presenting a single layer of structural domains. By scanning the beam in the laboratory frame, the projected overlap after the beam displacement is symmetric with equal step-sizes within the detector plane (a'b' = −a''b'') for the specular case. Reprinted with permission from Burdet *et al.*, Phys. Rev. B **96**(1), 014109 (2017). Copyright 2017 American Physical Society.

theorem in diffraction and tomography are described previously in the literature.[79,80] BPP considers the projection of the X-ray illumination volume, along the k_f direction, that is, the exit wave function propagation direction onto the detector plane, in the following way: $\int (P(r - r_j)^* O(r) dk_f)$, where dk_f is the vectorial integration element, P and O are the complex functions of the probe and the object, respectively, r is the 3D real-space lattice vector, and r_j represents the successive positions of the probe function.

To make BPP valid in such a way that a 2D intensity pattern in the Bragg geometry can be used to reconstruct a 2D real-space object complex function,[75–78] analogous to that being regularly used in the 2D forward geometry ptychography formalism, the projection of the X-ray illumination volume, along the exit wave function propagation direction onto the detector plane has to be rewritten as the following expression: $\int (P(r - r_j) dk_f) * \int (O(r) dk_f)$, where both the probe and the object terms will be reduced to 2D quantities. Under this 3D to 2D transformation, some strong requirements are needed so that the mathematical simplified transformations can hold.[75] The main requirements including (1) the 2D structures in the thin film under study are projections along the X-ray probe direction and (2) the probe illumination sizes on the sample are much bigger than the sample thickness (invariance of the film structures along the probe illumination integration direction; in other words, the structure in the thickness direction of the sample, which is composed to be a single domain of structural information, should not vary across the probe illuminated area on the sample). The successful BPP to date on phase-shifted domains in the thin film has been conducted on a sample with only a single information layer within the thickness direction.[72] In Sec. III (Low-dimensional Materials Science examples for X-ray ptychography), some of the most prominent physics examples are discussed and how X-ray Bragg ptychography could be employed as an important characterization tool in the foreseeable future is assessed.

III. LOW-DIMENSIONAL MATERIALS SCIENCE EXAMPLES FOR X-RAY PTYCHOGRAPHY
A. Charge, conductivity, and strain

Nanowires (NWs) are usually synthesized via the bottom-up or top-down approaches, such as chemical vapor deposition (CVD) or electron beam lithography, respectively. Semiconductor nanowires are of particular importance in the solid state electronics applications, such as silicon or germanium nanowire-based field-effect transistors (FETs) and nanowire-based photovoltaic solar cells.[81–83] There has been growing interest in gaining a better understanding of the undesirable mechanisms such as the electromigration in silicon-based transistors. Electron migration results in the connection failure in circuit interconnects in integrated circuits (ICs). The aim is to strengthen the properties of semiconductor devices and improve the performance of the devices in general.

A new class of III-V nanowire heterostructures have been under intense research in the past decade. New devices have demonstrated significant improvements in the efficiency and the performance compared with that of the homogeneous nanowires.[84,85] Heterostructured nanowire-based devices with various structural complexities exhibit different structural, optical, and electrical transport properties. In these complex systems, the generation and relaxation of compressive (tensile) strains, local dislocations, or defects are of the fundamental importance; the ability to image the strains *in situ* is a key step towards

mastering growth parameters in the manipulation of the physical properties of nanowire heterostructure systems. It is well known that large numbers of structural defects are usually generated as a result of the complexity of the heterostructure system due to the unpredictable interfacial structures developed along the nanowire growth axis. Ptychography with high spatial and spectroscopic sensitivities may provide solutions to those critical questions.

The ability to select the arbitrarily defined field-of-view in ptychography allows researchers to select the region of scan areas to match the sizes/shapes of the nanostructures under study. Even when nanowires are of significantly higher aspect ratio and substantial elongation, ptychography is capable of inverting the structures of these nanowires without difficulties. The only concern is that the data acquisition time required to image large nanowires can be relatively long. However, using partially coherent X-rays[40–43] and fly-scan ptychography[44,45] in the diffraction-limited synchrotron facilities, one can drastically reduce the total data acquisition time by using multi-modal ptychography.[40,41,43,86]

For investigations of single crystalline nanowires, the sensitivity of Bragg ptychography can enable the recovering of complete 3D strain tensor within a nanowire, and this has been successfully performed with CXDI at a relatively high spatial resolution on a ZnO nanorod.[87] Robinson and Harder have comprehensively demonstrated the mathematical derivation of the complete strain retrieval using CXDI in Bragg geometry.[20] This concept can be extended to Bragg ptychography, although applying it to 3D Bragg ptychography can be especially challenging. The associated strain tensors within single crystalline nanowires/thin films can be quantitatively reconstructed by using Bragg ptychography. Some exemplary demonstrations of Bragg ptychography studies on the single crystal structures include the SiGe-on-SOI structure,[78] the nanoscale semiconductor heterostructures,[76] and a single InGaN/GaN core–shell nanowire.[88] 2D BPP has been used for imaging the surfaces of the crystal truncation rod[89] in a recent study. BPP on niobium phase domains has been recently demonstrated[72] with a spatial resolution of about 37 nm. In order to satisfy the projection approximation, the thin film thickness was much smaller than the X-ray probe size on the sample.[75] Researchers have combined both Bragg CXDI and BPP to study core-shell-shell nanowires GaAs/(In,Ga)As/GaAs nanowires (NWs).[90] In the projection case, where the X-ray illuminating area is relatively large due to the small incident angle, this condition can be satisfied when thin film samples are of thickness of hundreds of nanometer. For Bragg ptychography in 3D geometry, there has been some remarkable breakthrough in the last few years, notably, the retrieval of 2D displacement fields from silicon, the identification of strains of nanowires on a silicon-on-insulator wafer[91] structure, strain mapping of an extended ZnO crystal,[92] silicon-on-insulator nanostructures,[93] an extended InP nanostructured layer bonded onto silicon,[94] and a new insight into nanoscale lattice behavior, strain fields, and structural defects by using 3D Bragg projection ptychography (3DBPP)[95] and multiangle BPP.[96] Figure 4[96] shows lattice displacements (encoded in the phase of the 3D reconstructions) within the multiple-angle (ma) BPP reconstruction of a single InGaAs nanowire; additionally, it displays the converted strain fields at the same position in one of the 2D projection slices of the 3D multiple-angle reconstructions on the nanowire. Another impressive study applied 3DBPP in a silicon-on-insulator nanostructure,[93] with the help of finite element models (FEM) to compare and assist the
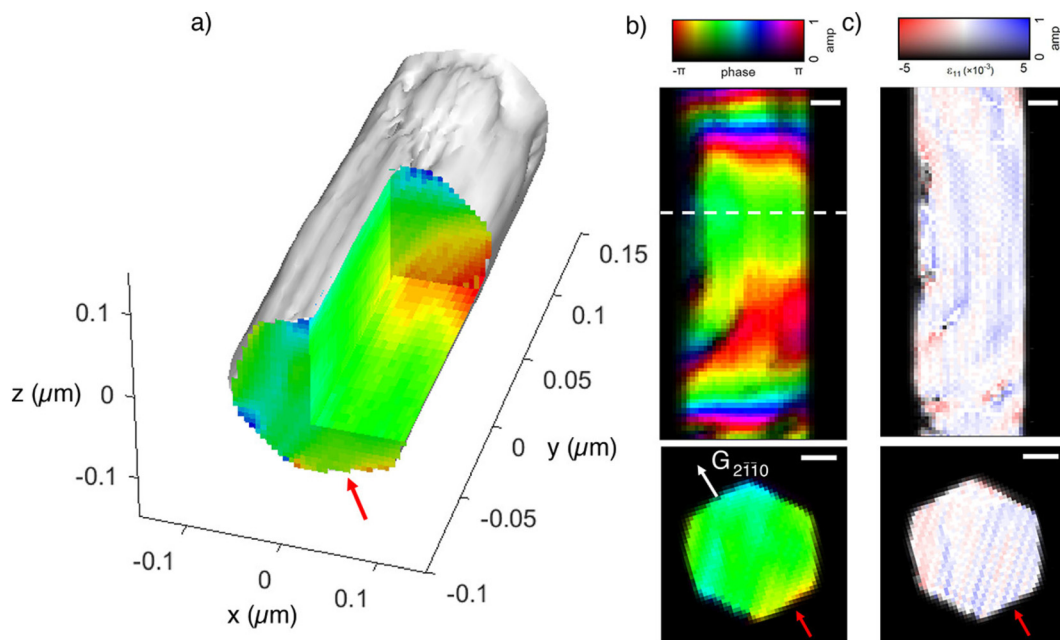
FIG. 4. maBPP reconstruction of the $2\bar{1}\bar{1}0$ peak. A cut into the (a) 3D reconstruction and (b) 2D cuts are taken from this volume. The cross-sectional cut was taken from the line marked (dashed white line). This reconstruction gives sensitivity to lattice displacement along $G_{2\bar{1}\bar{1}0}$ (white arrow). The same 2D cross-sections are converted to strain (ϵ_{11}) (c). Pixels at which the strain-derivative wraps over in phase are not shown because they are nonphysical. The red arrows identify the NW facet that was adhered to the Si substrate. All scale bars are 50 nm. Reprinted with permission from Hill *et al.*, Nano Lett. **18**(2), 811–819 (2018). Copyright 2018 American Chemical Society.
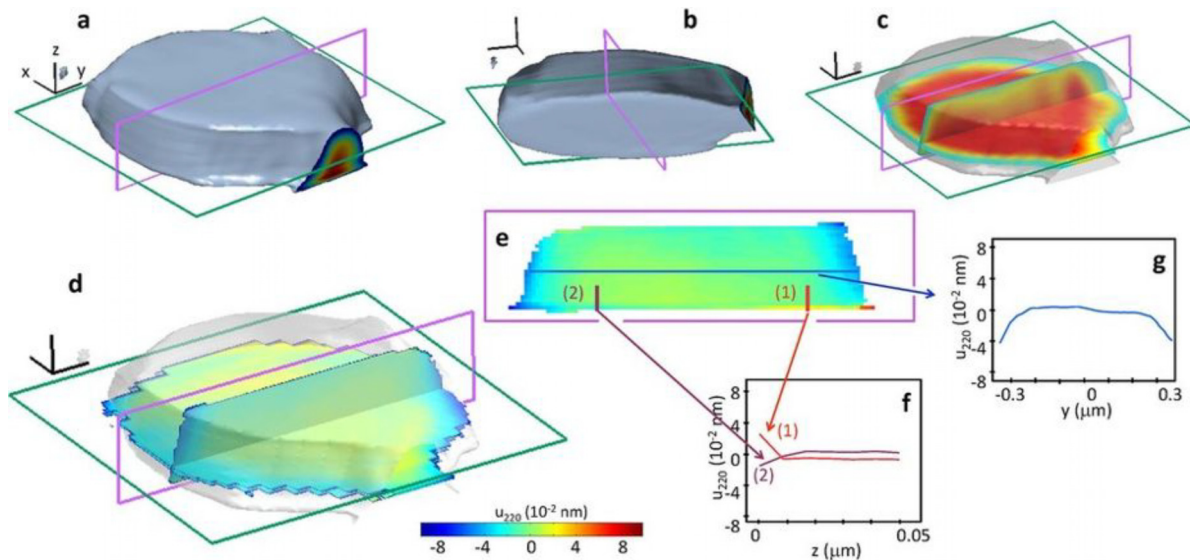

FIG. 5. (a) 3D isosurface plot rendition of the retrieved crystalline SOI structure density, shown in the laboratory frame (threshold at 30%). The length of the frame black lines corresponds to 0.1 μm. (b) Same as (a), other view. (c) Orthogonal 2D cuts of the density. (d) Orthogonal 2D cuts (2D slicing that is perpendicular with respect to the direction of the displacement field component…) of the displacement field component U_{220}. The color scale used to plot the U_{220} images is given at the bottom. (e) 2D cut in the (**y,z**) plane extracted from (d). The specific behavior of U_{220} is emphasized in the 1D cuts taken along the colored lines in (f) and (g). Reprinted with permission from Chamard *et al.*, Sci. Rep. **5**, 9827 (2015). Copyright 2015 Macmillan Publishers Ltd.

data analyses and interpretations. Figure 5[93] displays the three-dimensional reconstructed amplitude and phase maps of a single 3D lithographically patterned silicon-on-insulator nanostructure by implementing 3DBPP. These works demonstrated the promising perspective of 3DBPP for the investigation of nanostructured semiconductor materials.

For studying nanostructures by transmission geometry ptychography, a previous research has demonstrated that ptychography can extract the chemical compositions from biological specimens.[97] Furthermore, a recent invention of near-edge X-ray refraction fine-structure microscopy, which was reported from studies at the Advanced Light Source,[58,98] is a new example of studying elemental mapping[97] of nano-battery materials using soft X-ray spectroscopy-ptychography.[99] The study utilized both absorption (β) and phase (δ) components of the refractive indices of nano-materials to calculate the chemical mapping of the materials with high phase sensitivities. This results in enhanced contrast in the chemical mapping of the same materials compared to that of absorption-only, using the same experimental parameters. The fundamental nature of the structural, physical, and chemical properties of high-performance batteries that are commonly used in the energy industry is particularly important for the design of next-generation energy devices.[100,101] Using spectroscopy-ptychography, researchers can obtain a better understanding of these properties as the technique is chemical, elemental, and phase sensitive. Figure 6 shows two-dimensional reconstructions of a nano-battery
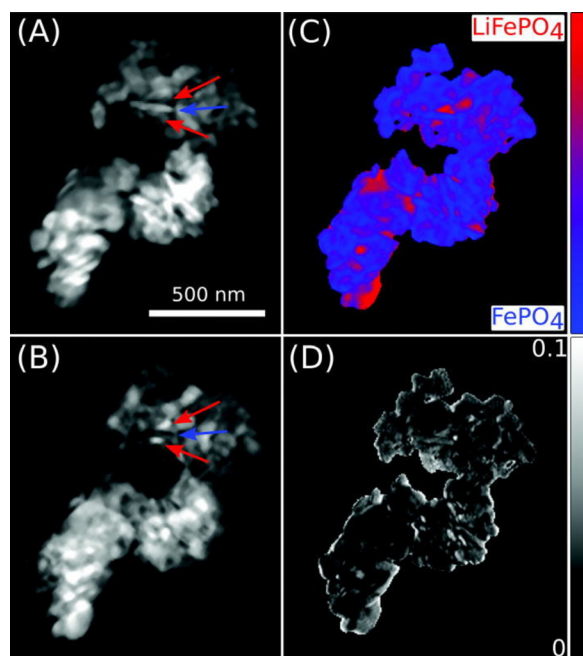

FIG. 6. (a) and (b) Experimental scattering contrast images of the partially discharged cathode agglomerate (50% state of charge) at two energies with peak contrast for the two components (X-ray energy of 708 eV for LiFePO$_4$ and 710 eV for FePO$_4$). The arrows point to lithium rich (red) and lithium poor (blue) regions. (c) Chemical composition map of the agglomerate obtained through mapping the experimental total contrast spectra of the two components. (d) R-factor map of the linear fitting shown in (c). Reprinted with permission from Appl. Phys. Lett. **110**(6), 063101 (2017). Copyright 2017 AIP Publishing LLC.

particle that is composed of both LiFePO$_4$ (LFP) and FePO$_4$ (FP) using both refraction and absorption components with enhanced chemical sensitivities by using a combination of principal component analysis and singular value decomposition (SVD).[102,103] Researchers have performed a similar study on catalyst particles,[104] and this has demonstrated that this technique is an advanced high-resolution versatile imaging tool for the investigation of nanostructures of batteries.

To extend the investigation of nano-scale battery particles in 3D, one latest study has shown this promising potential in the 3D structural retrieval. Figure 7[11] shows the three-dimensional quantitative chemical phase distribution of an individual nano-particle by soft X-ray PXCT. The chemical map of the nano-particle investigated has three components: LiFePO$_4$-rich, mixed of both LiFePO$_4$-rich and FePO$_4$-rich components, and FePO$_4$-rich, and each of the components can be described as linear equations. As a result, the relative compositions of LiFePO$_4$-rich and FePO$_4$-rich can be used to retrieve the quantitative 3D distribution of the iron oxidation state. Similarly, in 3D semiconductor devices, researchers have successfully reconstructed nanostructures within 3D integrated circuits[4,10,105] using PXCT in recent studies, and this paves a way for the high-throughput high-resolution tomographic nanoscale structural characterization studies in the military and semiconductor industries.

Following the great success in the recent ptychography studies on nanowires and nanostructures (in both transmission and Bragg geometries), there has been growing demands for using ptychography to further investigate nanoscale materials for groundbreaking discoveries. Future studies on Bragg ptychography should focus on key unsolved physics problems, such as first order phase transitions (FOPTs) in materials such as BaTiO$_3$ and similar single crystalline oxides.[106] FOPTs are typically of discontinuous nature, that is, the first derivatives of Gibbs free energy (G) with respect to temperature or pressure are discontinuous by definition. On the other hand, the second-order phase transitions are continuous in the first derivatives of G, and they display discontinuity in the second derivatives of G with respect to either the temperature or the pressure of the systems under investigation. BaTiO$_3$ at the ambient pressure undergoes FOPTs from cubic, tetragonal, orthorhombic to rhombohedral crystallographic structures from the highest to the lowest phase transition temperatures. Similarly, in vanadium dioxide, the electronic insulator-to-metal transition (IMT) suggests measureable structural changes[107] from the monoclinic phase at lower temperature to the rutile phase at higher temperature. The co-existence of both competing ferromagnetic and anti-ferromagnetic domains through the transition process follows in parallel with a commensurate expanded lattice. The open question asks what role lateral mismatch induced strain plays in the nucleation and growth behaviour of ferromagnetic to anti-ferromagnetic transition. A better understanding of the FOPT mechanisms allows us to engineer and control the phase transitions for high-performance device applications. The crystallographic lattice strains that are caused by the crystal lattice perturbations are also important for the manipulation and the control of phase transitions in the magneto-elastic systems. BPP is capable of detecting the phase shifts of tens of nanometers and the lattice displacements of up to a single atomic lattice constant for achieving pico-meter strain sensitivity because of the nature of the long-ranged strain states. Therefore, the detailed structural evolution arising from FOPTs can be detected and observed using Bragg geometry ptychography with X-rays.
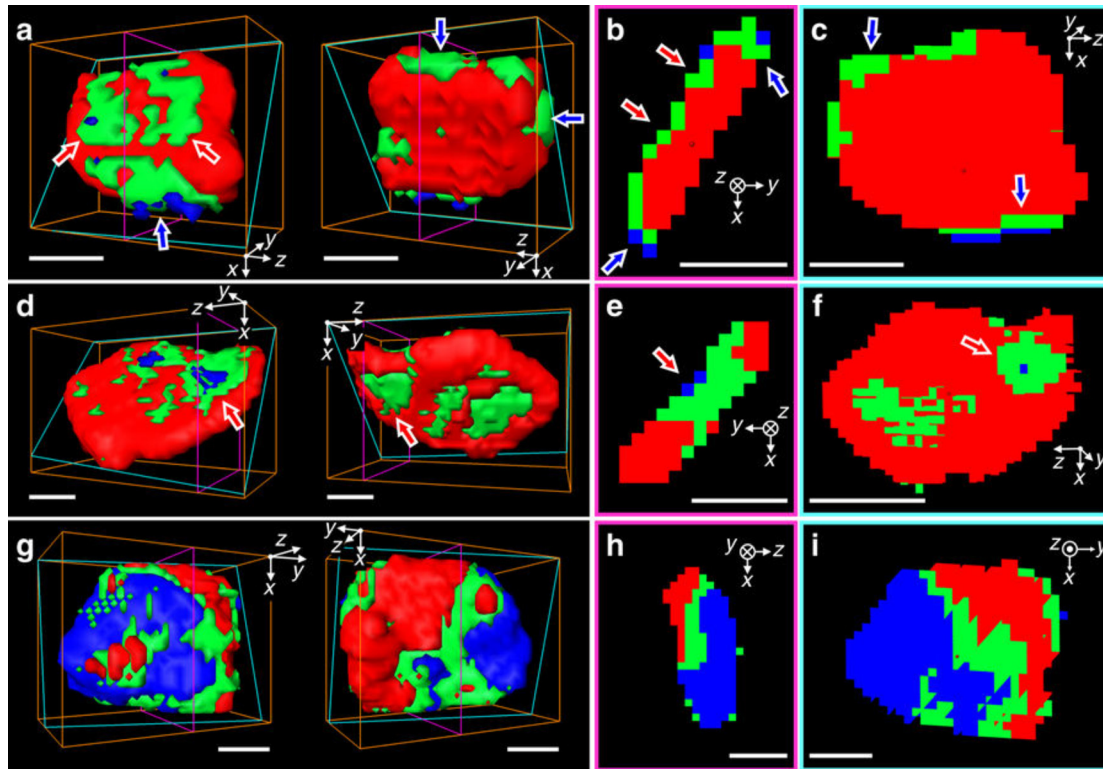
FIG. 7. Representative three-dimensional (3D) chemical phase distribution of individual particles of $LiFePO_4$-rich, mixture of both $LiFePO_4$-rich and $FePO_4$-rich components, or $FePO_4$-rich. (a), (d), and (g) Front (left) and backside (right) views of the isosurface of three chemical components. Cross-sectional views along the thickness direction [(b), (e), and (h)] and along the large face [(c), (f), and (i)]. The cross-sectional planes are indicated as magenta and cyan colored boxes in 3D isosurface plots. The red, green, and blue indicate LFP-rich, mixed, and FP-rich voxels, respectively. All scale bars are 50 nm. Reprinted with permission from Yu *et al.*, Nat. Commun. **9**(1), 921 (2018). Copyright 2018 Macmillan Publishers Ltd.

B. Magnetism and ferroelectricity

Ferroelectric and magnetic materials are characterized by a long-range ordering of atoms and electron spins and the emergence of a polarization and magnetization, respectively. The close relationship between atomic (structural and chemical) and microscopic (magnetic and ferroelectric) properties ideally requires a highly sensitive probe to visualize the microscopic properties, such as domains, domain walls (DWs), and spin current, at the (sub-)nano scale. This becomes even more evident in heterogeneous systems with imperfections, such as interfaces, amorphous films, granular films, nanowires, and nanoparticles.[108–111] Additionally, the polarization and magnetization themselves may form 3D non-collinear structures, such as domain walls, vortices, Skyrmions,[112–117] and Hopfions.[118,119] In fact, recent years have seen tremendous efforts to explore non-collinear structures in view of both basic sciences and use-inspired research for sensing, neuromorphic computing, and data storage applications. It is worth to note that despite distinct underlying mechanisms of magnetism (exchange interaction) and ferroelectricity (atomic displacement), both reveal to great extent the same large variety of non-collinear structures. While the advent of 3D nanomagnetism[120] and 3D nanoferroelectricity has been contingent on the advancement of synthesis science and theory, their future will most likely be determined by imaging techniques providing 3D spatial resolution at the sub-nanoscale to further tailor properties.

The ability to manipulate extrinsic effects to improve the piezoelectric properties has brought attention to the research field of complex electronic systems and multiferroics.[121,122] One of the key aims of the research is to directly characterize and image domain structures, especially those associated with phase transitions and magnetic heterogeneities. Obtaining a greater understanding of the structural evolution of domains under various external stimuli is crucial for the next-generation ferroelectric or ferromagnetic device applications. It is well-known that the piezoelectric constant becomes maximal when specific crystallographic orientations along the c-axis of ferroelectric crystals, such as $BaTiO_3$, are designated. The specific crystallographic orientation ensures the highest intrinsic piezoelectric constant, which is directly related to the material properties. Discovering how the extrinsic piezoelectric properties within a piezoelectric system occur is possible using high-resolution X-ray imaging. It is suggested that in ferroelectric materials with 90° DWs, narrowing the width of the DWs while maintaining the ratio to domain size has drastically increased piezoelectric constants.[123] Furthermore, in ferroelectric materials, piezoelectric domain properties can be engineered by applying an external electrical field and temperature.[124] Using BPP, it was shown on the example of single-crystal ferroelectric thin films[77] that the domain size, domain wall width, and type, e.g., 90° or 180° domain walls, can be tuned and selected according to the electrical field voltage vs.

temperature phase diagrams. The challenge with visualizing the internal structure of ferroelectric domain walls, typically done with high-resolution scanning transmission electron microscopy, is the spatial confinement to a few unit cells (<5 nm), which could be overcome by taking advantage of the high spatial resolution of X-ray ptychography.

A similar dependence holds for magnetic thin films, where the magnetization configuration can be tailored according to the magnetic field vs. temperature phase diagram. Although magnetic DWs are slightly broader than their ferroelectric counterpart, they typically resemble complex non-collinear spin textures. While traditionally magnetic DWs were simplified as 1D boundary regions, modern magnetism has recognized the importance of their internal structure, namely, type, symmetry, chirality, and thickness profile, particularly in view of the advent of spintronics[125,126]—a novel concept of electronics harnessing electron spins. To this end, manipulating DWs via spin current, exchange interactions, bias fields, temperature, composition, and heterogeneity has become one of the leading themes. X-ray ptychography with X-ray magnetic circular dichroism (XMCD) has the potential to visualize the element specifically the internal structure of DWs at the nanoscale, ultimately offering the retrieval of the 3D magnetization vector field. Acquiring two series with opposite X-ray polarization and subsequent division or tuning the energy through the resonance allows for further correlating the magnetization configuration with heterogeneities. Figure 8 shows exemplarily the phase and amplitude contrast of out-of-plane magnetized SmCo$_5$ thin films near

the cobalt L_3 absorption edge with a spatial resolution down to about 10 nm.[59] A similar spatial resolution was reported for FeGd thin films[127] and magnetotactic bacteria[117,118] near the iron L_3 edge. A recent example on imaging Skyrmions by soft X-ray ptychography[128] has shown promising potential in the development of this scientific area. These works were in good agreement with XMCD studies using other X-ray imaging and scattering techniques, such as X-ray resonant holography[15] and resonant soft X-ray scattering (RSoXS).[119,120] The great advantage of soft X-rays compared to hard X-rays is the probing of dipole transitions, which provide a significantly enhanced magnetic contrast at the expense of a limited sample thickness of about 100 nm. However, this limitation did not hinder the application of hard X-ray ptychography to study films but extends the application potential towards 100's of nanometer thick samples and rare-earth elements.[129,130] Figure 9 displays hard X-ray ptychography results near the gadolinium L_3 edge on a 500 nm-thick FeGd film, conducted at the cSAXS beamline, Swiss Light Source, which later on demonstrated magnetic hard X-ray PXCT.[131]

The typical setup of normal and oblique incidence (sensitivity) for magnetic films with perpendicular and in-plane magnetic anisotropy, respectively, provides means to study the domain morphology, magnetization reversal processes, and element specificity. However, it is not possible to retrieve satisfying information on the internal structure of DWs. This is due to the spatial confinement, three-dimensionality (rapidly varying magnetization components), and
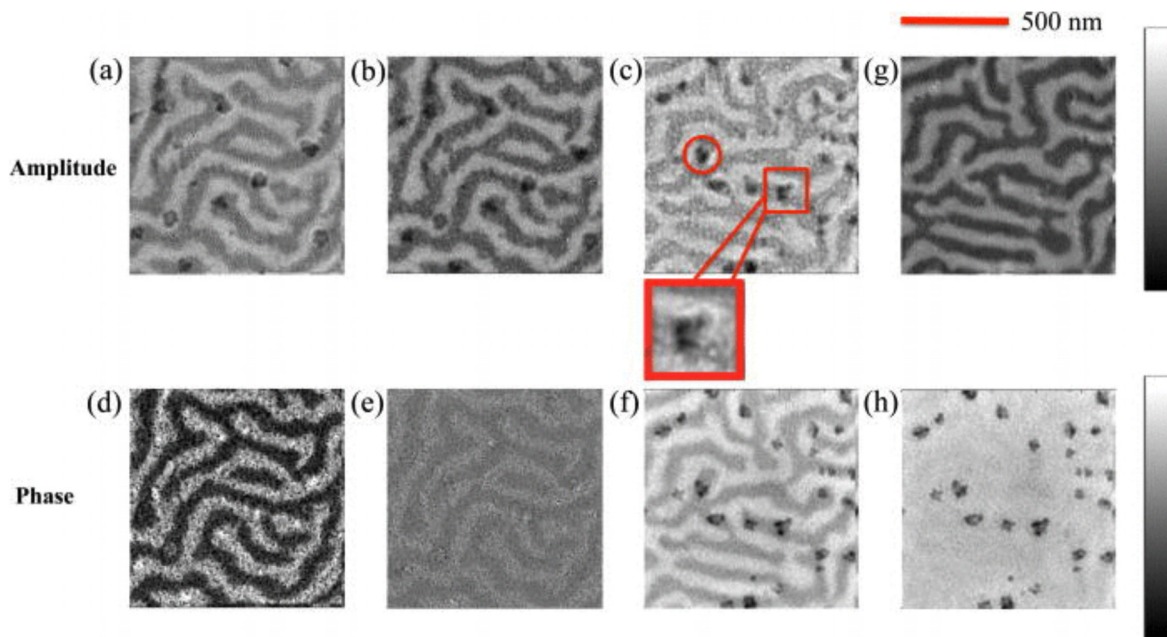

FIG. 8. Reconstructed amplitude (a)–(c) and phase (d)–(f) components of three X-ray energies of the SmCo$_5$ thin film sample in transmission geometry. (a) and (d) Reconstructions at an X-ray energy of 778 eV; (b) and (e) reconstructions at an X-ray energy of 778.6 eV; and (c) and (f) reconstructions at an X-ray energy of 780 eV. The red open circle and square (with a red zoomed open square) indicate the inclusions present in the thin film sample. Note that in (d), the inclusions have opposite contrast (white color), indicating that the phase contrast is reversed compared to phase contrast in (f). The gray-scale bar is in the range of −0.2 to 0.5 rad. The phase component of the refractive index changes the sign when going through the absorption component maximum. (g) Difference of left- and right-polarized reconstructed phase images at 780 eV X-ray energy taken at the position shown in (c) and (f). The gray-scale bar is in the range of −0.4 to 0.4 rad. (h) Sum of left- and right-polarized reconstructed phase images at an X-ray energy of 780 eV. The gray-scale bar is in the range of 0 to 1.2 rad. Reprinted with permission from Appl. Phys. Lett. **108**(9), 094103 (2016). Copyright 2016 AIP Publishing LLC.
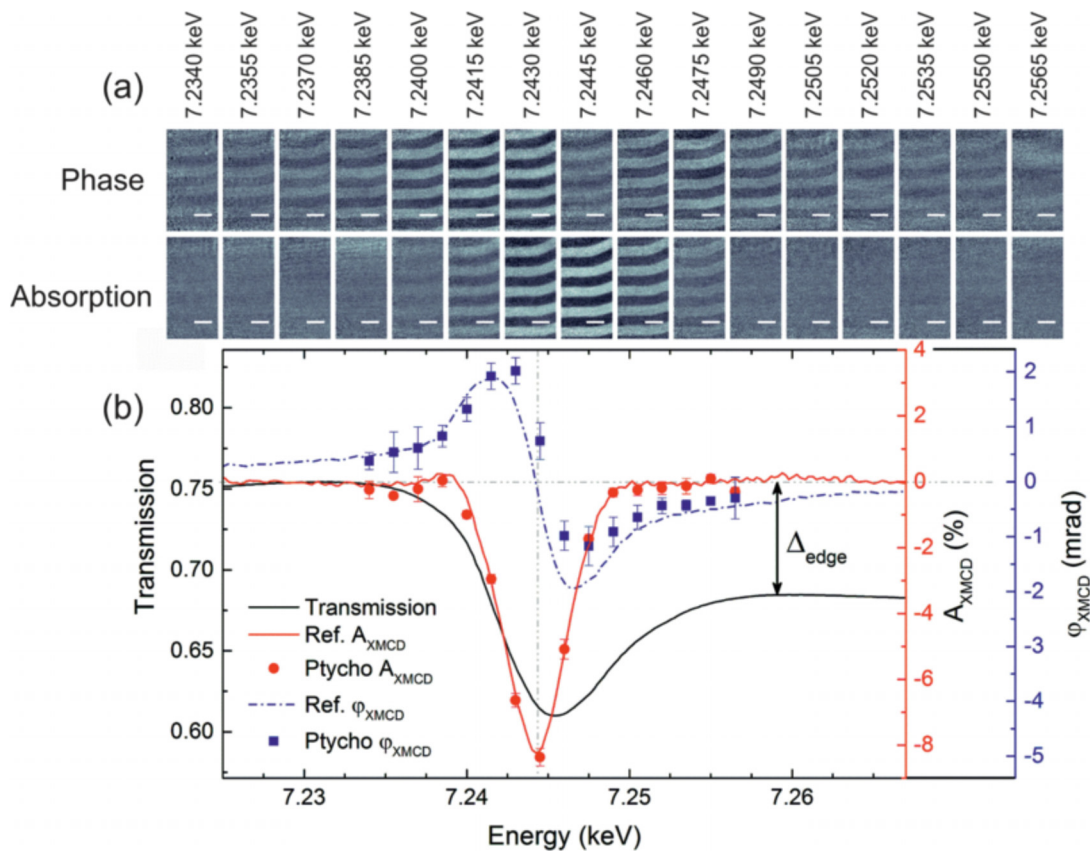
FIG. 9. (a) XMCD ptychographic images of the magnetic domain configuration of the FeGd film obtained from the difference taken between images measured with Circular-Right and Circular-Left polarized light. Phase contrast (upper row) and absorption contrast (lower row) are given for a number of photon energies spanning the Gd L_3 edge. Scale bars represent 1 μm. (b) The absorption XMCD (red circles) and phase XMCD (blue squares) signal extracted from the images is presented, providing a direct comparison of the phase and absorption signals. The XMCD data are compared with a reference absorption XMCD spectrum (red line) measured in fluorescence on a similar sample and the corresponding phase XMCD reference spectrum calculated with the Kramers-Kronig relations (dashed blue line). A transmission spectrum of the sample (black line) is provided as a reference. Reprinted with permission from Donnelly et al., Phys. Rev. B **94**(6), 064421 (2016). Copyright 2016 American Physical Society.

sensitivity to only one magnetization component. In other words, the DW type, chirality, and symmetry cannot unambiguously be identified for simple cases (Fig. 10)[135] or more complicated hybrids.[132] This limitation can be overcome with Lorentz microscopy, which allows for retrieving the two in-plane magnetization components or tilting the sample around symmetry axes of the sample/DW and correlating with simulations or performing tomography. The first prototypical demonstration of magnetic X-ray tomography was given on the example of a uniaxial tubular system that enabled a reconstruction from one tilt series.[133] The critical limitation to one single tilt axis perpendicular to the X-ray propagation direction (sensitivity) was due to spatial restrictions of the experimental setup to about 1 mm between the sample and vacuum windows. Switching to either vacuum soft X-ray microscopes or hard X-ray microscopes has empowered the community to lift those limitations and carry out true 3D magnetic X-ray tomography. Despite a significant boost in research activities and ongoing efforts at various synchrotron radiation facilities, thus far only one more demonstration was reported utilizing PXCT.[131] In their work, Donnelly et al. impressively visualize the 3D magnetization vector field

of a soft-magnetic GdCo micropillar (5 μm in diameter) with a spatial resolution of about 100 nm (Fig. 11). In spite of the relatively poor spatial resolution, they were able to identify Bloch points and Anti-Bloch points based on the surrounding magnetization configuration,[131] similar to Lorentz microscopy in 2D.[132] The combination of ptychography and hard X-rays benefited spatial resolution, enlarged the attenuation length, and provided plenty of space for implementing multiple rotation axes. The highly sensitive phase contrast of X-ray ptychography compensated in parts the significantly weaker XMCD contrast of non-dipole transitions at the expense of data acquisition and analysis. Establishing magnetic X-ray tomography as a main stream tool faces three challenges: (i) designing and upgrading more end stations; (ii) improving reconstruction algorithms in view of computation, accuracy, and universality; and most importantly (iii) harnessing fully coherent beams. As ptychography relies on coherence, its performance is currently very limited and will experience a mind-blowing boost (two orders of magnitude) once the ongoing upgrades to diffraction limited light sources with much higher flux of coherent beams are complete in the next one to two decades. Iterative retrieval algorithms
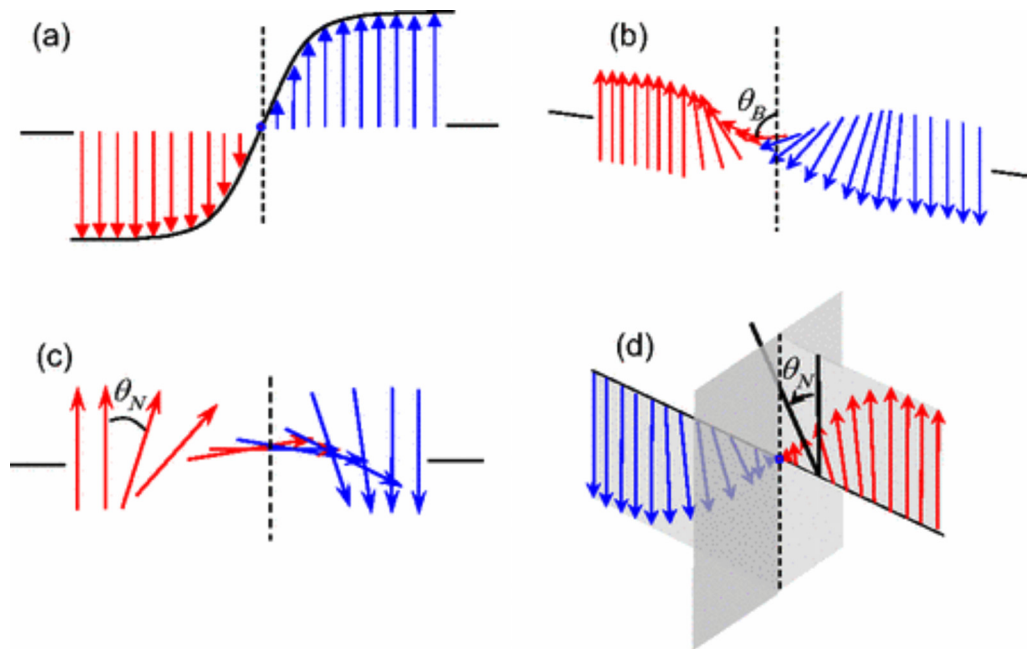
FIG. 10. Different types of domain walls: (a) Ising type, (b) Bloch type, (c) Néel type, and (d) mixed Ising-Néel type walls. A mixed Ising-Bloch type would look similar to (d) except that the rotation (θ_B) would be out of the plane of the polarization vector. Reprinted with permission from Lee *et al.*, Phys. Rev. B **80**(6), 060102 (2009). Copyright 2009 American Physical Society.

for 3D reconstruction have seen a significant improvement in both computation and accuracy.[134]

IV. CONCLUSION AND FUTURE OUTLOOKS

Ptychography is a powerful tool to visualize nanostructures in hard-condensed matter in both reflection (Bragg geometry) and transmission (forward geometry) with high spatial resolution and quantitative highly sensitive phase contrast. Electron ptychography relying on scanning transmission electron diffraction and X-ray ptychography with STXM are two representatives of the family of coherent imaging complementing X-ray interferometry and X-ray and electron holography that take advantage of the non-destructive phase contrast properties and phase retrieval to unveil features at the nanoscale. The X-ray ptychography with element specificity is a strong contender for imaging materials with a large scattering cross-section since local heterogeneities can be investigated in a large field-of-view with high experimental data statistics. Researchers are now able to investigate chemical and physical phenomena in nanoscale systems, e.g., semiconductors, superconductors, batteries, ferroelectrics, ferromagnets, and multiferroics, in both transmission and reflection using resonant X-ray absorption of soft or hard X-rays. The current focus on demonstrating ptychography on primarily prototypical systems will shift toward complex systems with real-world conditions. Future directions in Bragg ptychography include *in-situ* and *operando* measurements of functional devices, e.g., strain evolution in ferroelectric and piezoelectric actuators. Understanding the influence of structural and chemical heterogeneities on the performance, i.e., charging and discharging, of nano-battery devices is one avenue for transmission X-ray ptychography. Facilitating time-resolved spectroscopy-ptychography measurements allows for

examining the structural and chemical transformation of battery oxide cathode materials as a function of (dis-)charging speed and for optimizing cycling and lifetime. Establishing magnetic X-ray ptychography as a main stream tool in foreseeable future calls for designing and upgrading end stations, efficient data acquisitions, and live post-processing to visualize magnetism-related textures and heterogeneities. Reconstructing the 3D vector fields of heterogeneities with tomographic imaging will be essential to explore 3D nano-magnetism and 3D nano-ferroelectricity in view of novel electronics succeeding CMOS technology.

The ongoing upgrades to diffraction limited light sources with much higher coherent beams, which are expected to be completed in the next one to two decades, will empower researchers to probe dynamics and fluctuations at time scales ranging down to femto seconds and to visualize heterogeneities in 3D using X-ray ptychography as a main stream characterization tool. Advancing synchrotron beamline environment stability, *in-situ* or *in-vivo* sample environments, ptychographic iterative algorithms, and X-ray detectors are further improvements to fully foster the coherent flux of diffraction limited light sources. Future developments of (CCD) detectors aim to increase the efficiency (sensitivity) and dynamic range in wide energy ranges, reduce pixel size, and improve energy resolution and count rate of photon-counting sensing areas by overcoming the bottleneck of charge-sharing effects and to minimize polarization issues for very high X-ray fluxes for direct-detection semiconductor materials. The inherent synergy of science and technology accompanying the transformation to diffraction-limited synchrotron facilities and 4th generation X-ray free electron laser sources around the world enables novel X-ray characterization techniques, next-generation devices, and applications to nanotechnology
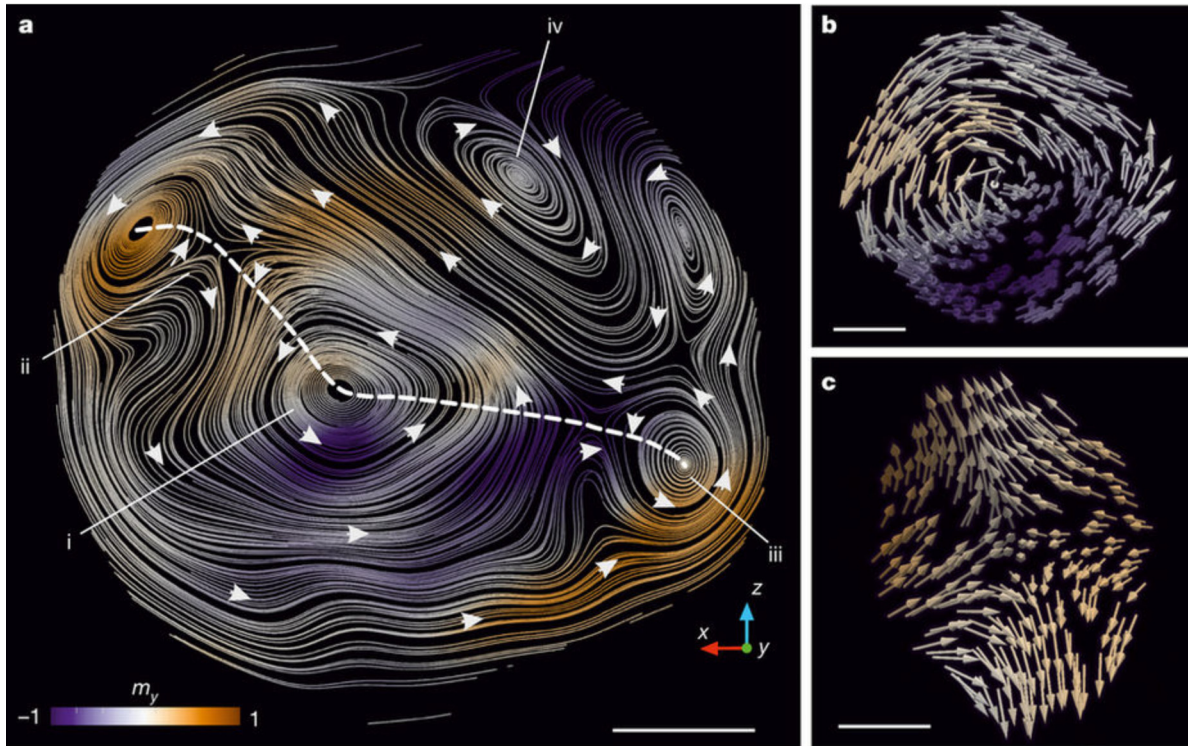
FIG. 11. (a) A section taken perpendicular to the long axis of a soft GdCo$_2$ magnetic cylinder sample is shown, in which the streamlines represent the x–z components of the magnetization and different magnetic structures can be identified. The diameter of the magnetic cylinder under this study is 5 μm. There are anticlockwise vortices, such as (i) and (iii), a clockwise vortex (iv), and antivortices, such as (ii), which occur between two vortices with the same vorticity. (b) and (c) The three-dimensional magnetic nanostructure of a vortex (i) and an antivortex (ii), respectively, is shown in more detail. A section of a cross-tie wall consisting of a succession of vortex and antivortex structures is indicated by the dashed white line in (a). Scale bars represent 1 μm in (a) and 300 nm in (b) and (c). Reprinted with permission from Donnelly *et al.*, Nature **547**(7663), 328–331 (2017). Copyright 2017 Macmillan Publishers Ltd.

and nanomaterials across life, chemical, physical, materials, and engineering sciences in an inter-/multi-disciplinary manner.

REFERENCES

[1] F. Pfeiffer, Nat. Photonics **12**(1), 9–17 (2018).
[2] D. A. Shapiro, Y.-S. Yu, T. Tyliszczak, J. Cabana, R. Celestre, W. Chao, K. Kaznatcheev, A. L. D. Kilcoyne, F. Maia, S. Marchesini, Y. S. Meng, T. Warwick, L. L. Yang, and H. A. Padmore, Nat. Photonics **8**(10), 765–769 (2014).
[3] J. Vila-Comamala, S. Gorelick, E. Färm, C. M. Kewish, A. Diaz, R. Barrett, V. A. Guzenko, M. Ritala, and C. David, Opt. Express **19**(1), 175–184 (2011).
[4] K. Shimomura, M. Hirose, and Y. Takahashi, Acta Crystallogr., Sect. A: Found. Adv. **74**(1), 66–70 (2018).
[5] A. Suzuki, S. Furutaku, K. Shimomura, K. Yamauchi, Y. Kohmura, T. Ishikawa, and Y. Takahashi, Phys. Rev. Lett. **112**(5), 053903 (2014).
[6] H. Öztürk, H. Yan, Y. He, M. Ge, Z. Dong, M. Lin, E. Nazaretski, I. K. Robinson, Y. S. Chu, and X. Huang, Optica **5**(5), 601–607 (2018).
[7] M. Dierolf, A. Menzel, P. Thibault, P. Schneider, C. M. Kewish, R. Wepf, O. Bunk, and F. Pfeiffer, Nature **467**(7314), 436–439 (2010).
[8] S. V. Venkatakrishnan, M. Farmand, Y.-S. Yu, H. Majidi, K. van Benthem, S. Marchesini, D. A. Shapiro, and A. Hexemer, IEEE Signal Process. Lett. **23**(7), 944–948 (2016).
[9] M. Holler, A. Diaz, M. Guizar-Sicairos, P. Karvinen, E. Farm, E. Harkonen, M. Ritala, A. Menzel, J. Raabe, and O. Bunk, Sci. Rep. **4**, 3857 (2014).
[10] M. Holler, M. Guizar-Sicairos, E. H. R. Tsai, R. Dinapoli, E. Müller, O. Bunk, J. Raabe, and G. Aeppli, Nature **543**, 402 (2017).
[11] Y.-S. Yu, M. Farmand, C. Kim, Y. Liu, C. P. Grey, F. C. Strobridge, T. Tyliszczak, R. Celestre, P. Denes, J. Joseph, H. Krishnan, F. R. N. C. Maia, A. L. D. Kilcoyne, S. Marchesini, T. P. C. Leite, T. Warwick, H. Padmore, J. Cabana, and D. A. Shapiro, Nat. Commun. **9**(1), 921 (2018).
[12] A. Scholl, F. Nolting, J. Stöhr, T. Regan, J. Lüning, J. W. Seo, J. P. Locquet, J. Fompeyrine, S. Anders, H. Ohldag, and H. A. Padmore, J. Appl. Phys. **89**(11), 7266–7268 (2001).

[13]W. Kuch, J. Gilles, S. S. Kang, S. Imada, S. Suga, and J. Kirschner, Phys. Rev. B **62**(6), 3824–3833 (2000).

[14]S. Eisebitt, J. Lüning, W. F. Schlotter, M. Lörgen, O. Hellwig, W. Eberhardt, and J. Stöhr, Nature **432**, 885 (2004).

[15]A. Scherz, W. F. Schlotter, K. Chen, R. Rick, J. Stöhr, J. Lüning, I. McNulty, C. Günther, F. Radu, W. Eberhardt, O. Hellwig, and S. Eisebitt, Phys. Rev. B **76**(21), 214410 (2007).

[16]J. Miao, P. Charalambous, J. Kirz, and D. Sayre, Nature **400**, 342–344 (1999).

[17]D. Shapiro, P. Thibault, T. Beetz, V. Elser, M. Howells, C. Jacobsen, J. Kirz, E. Lima, H. Miao, A. M. Neiman, and D. Sayre, Proc. Natl. Acad. Sci. U. S. A. **102**(43), 15343–15346 (2005).

[18]X. Huang, J. Nelson, J. Kirz, E. Lima, S. Marchesini, H. Miao, A. Neiman, D. Shapiro, J. Steinbrener, A. Stewart, J. Turner, and C. Jacobsen, Phys. Rev. Lett. **103**(19), 198101 (2009).

[19]E. Lima, L. Wiegart, P. Pernot, M. Howells, J. Timmins, F. Zontone, and A. Madsen, Phys. Rev. Lett. **103**(19), 198102 (2009).

[20]I. Robinson and R. Harder, Nat. Mater. **8**(4), 291–298 (2009).

[21]T. Sun, Z. Jiang, J. Strzalka, L. Ocola, and J. Wang, Nat. Photonics **6**, 586 (2012).

[22]D. Sayre, Acta Crystallogr. **5**, 843 (1952).

[23]M. Dierolf, O. Bunk, S. Kynde, P. Thibault, I. Johnson, A. Menzel, K. Jefimovs, C. David, O. Marti, and F. Pfeiffer, Europhys. News **39**(1), 22–24 (2008).

[24]S. Roy, D. Parks, K. A. Seu, R. Su, J. J. Turner, W. Chao, E. H. Anderson, S. Cabrini, and S. D. Kevan, Nat. Photonics **5**, 243–245 (2011).

[25]P. Hessing, B. Pfau, E. Guehrs, M. Schneider, L. Shemilt, J. Geilhufe, and S. Eisebitt, Opt. Express **24**(2), 1840–1851 (2016).

[26]W. Hoppe, "Beugung im inhomogenen Primärstrahlwellenfeld. I. Prinzip einer Phasenmessung von Elektronenbeugungsinterferenzen," Acta Crystallogr., Sect. A: Found. Adv. **25**(4), 495 (1969).

[27]G. Xiong, O. Moutanabbir, M. Reiche, R. Harder, and I. Robinson, Adv. Mater. **26**(46), 7747–7763 (2014).

[28]J. Rodenburg, A. Hurst, A. Cullis, B. Dobson, F. Pfeiffer, O. Bunk, C. David, K. Jefimovs, and I. Johnson, Phys. Rev. Lett. **98**(3), 034801 (2007).

[29]P. Thibault, M. Dierolf, A. Menzel, O. Bunk, C. David, and F. Pfeiffer, Science **321**(5887), 379–382 (2008).

[30]K. A. Nugent, Adv. Phys. **59**(1), 1–99 (2010).

[31]P. Thibault, M. Dierolf, O. Bunk, A. Menzel, and F. Pfeiffer, Ultramicroscopy **109**(4), 338–343 (2009).

[32]A. M. Maiden and J. M. Rodenburg, Ultramicroscopy **109**(10), 1256–1262 (2009).

[33]V. Elser, J. Opt. Soc. Am. A **20**, 40–55 (2003).

[34]D. R. Luke, Inverse Probl. **21**(1), 37–50 (2005).

[35]S. Marchesini, H. Krishnan, B. J. Daurer, D. A. Shapiro, T. Perciano, J. A. Sethian, and F. R. N. C. Maia, J. Appl. Crystallogr. **49**(4), 1245–1252 (2016).

[36]P. Godard, M. Allain, V. Chamard, and J. Rodenburg, Opt. Express **20**(23), 25914–25934 (2012).

[37]P. Thibault and M. Guizar-Sicairos, New J. Phys. **14**(6), 063004 (2012).

[38]M. Odstrčil, A. Menzel, and M. Guizar-Sicairos, Opt. Express **26**(3), 3108–3123 (2018).

[39]M. Stefano, S. Andre, Y. Chao, W. Hau-tieng, and M. Filipe, Inverse Probl. **29**(11), 115009 (2013).

[40]J. N. Clark, X. Huang, R. J. Harder, and I. K. Robinson, Phys. Rev. Lett. **112**(11), 113901 (2014).

[41]P. Thibault and A. Menzel, Nature **494**(7435), 68–71 (2013).

[42]N. Burdet, X. Shi, D. Parks, J. N. Clark, X. Huang, S. D. Kevan, and I. K. Robinson, Opt. Express **23**(5), 5452–5467 (2015).

[43]B. Enders, M. Dierolf, P. Cloetens, M. Stockmar, F. Pfeiffer, and P. Thibault, Appl. Phys. Lett. **104**(17), 171104 (2014).

[44]X. Huang, K. Lauer, J. N. Clark, W. Xu, E. Nazaretski, R. Harder, I. K. Robinson, and Y. S. Chu, Sci. Rep. **5**, 9074 (2015).

[45]J. Deng, Y. S. G. Nashed, S. Chen, N. W. Phillips, T. Peterka, R. Ross, S. Vogt, C. Jacobsen, and D. J. Vine, Opt. Express **23**(5), 5438–5451 (2015).

[46]Y. S. G. Nashed, T. Peterka, J. Deng, and C. Jacobsen, Procedia Comput. Sci. **108**, 404–414 (2017).

[47]B. Enders, K. Nowrouzi, H. Krishnan, S. Marchesini, J. Park, Y.-S. Yu, and D. A. Shapiro, Microsc. Microanal. **24**(S2), 56–57 (2018).

[48]Z. Dong, Y.-L. Fang, X. Huang, H. Yan, S. Ha, W. Xu, Y. S. Chu, S. I. Campbell, and M. Lin, *High-Performance Multi-Mode Ptychography Reconstruction on Distributed GPUs* (2018).

[49]R. W. Harrison, J. Opt. Soc. Am. A **10**(5), 1046–1055 (1993).

[50]A. Altomare, G. Cascarano, C. Giacovazzo, A. Guagliardi, M. C. Burla, G. Polidori, and M. Camalli, J. Appl. Crystallogr. **27**(3), 435–436 (1994).

[51]H. A. Hauptman, Rep. Prog. Phys. **54**(11), 1427 (1991).

[52]M. Stockmar, P. Cloetens, I. Zanette, B. Enders, M. Dierolf, F. Pfeiffer, and P. Thibault, Sci. Rep. **3**, 1927 (2013).

[53]B. A. Pound, J. L. Barber, K. Nguyen, M. C. Tyson, and R. L. Sandberg, Phys. Rev. B **96**(5), 054104 (2017).

[54]H. D. Bale and P. W. Schmidt, Phys. Rev. Lett. **53**(6), 596–599 (1984).

[55]M. Cammarata, M. Levantino, F. Schotte, P. A. Anfinrud, F. Ewald, J. Choi, A. Cupane, M. Wulff, and H. Ihee, Nat. Methods **5**, 881 (2008).

[56]H. Mimura, S. Handa, T. Kimura, H. Yumoto, D. Yamakawa, H. Yokoyama, S. Matsuyama, K. Inagaki, K. Yamamura, Y. Sano, K. Tamasaku, Y. Nishino, M. Yabashi, T. Ishikawa, and K. Yamauchi, Nat. Phys. **6**, 122–125 (2010).

[57]J. Cesar da Silva, A. Pacureanu, Y. Yang, S. Bohic, C. Morawe, R. Barrett, and P. Cloetens, Optica **4**(5), 492–495 (2017).

[58]M. Farmand, R. Celestre, P. Denes, A. L. D. Kilcoyne, S. Marchesini, H. Padmore, T. Tyliszczak, T. Warwick, X. Shi, J. Lee, Y.-S. Yu, J. Cabana, J. Joseph, H. Krishnan, T. Perciano, F. R. N. C. Maia, and D. A. Shapiro, Appl. Phys. Lett. **110**(6), 063101 (2017).

[59]X. Shi, P. Fischer, V. Neu, D. Elefant, J. C. T. Lee, D. A. Shapiro, M. Farmand, T. Tyliszczak, H.-W. Shiu, S. Marchesini, S. Roy, and S. D. Kevan, Appl. Phys. Lett. **108**(9), 094103 (2016).

[60]I. K. Robinson, Z. Kristallogr. Supplements **2008**(27), 27–35.

[61]T. B. Edo, D. J. Batey, A. M. Maiden, C. Rau, U. Wagner, Z. D. Pešić, T. A. Waigh, and J. M. Rodenburg, Phys. Rev. A **87**(5), 053850 (2013).

[62]D. J. Batey, T. B. Edo, C. Rau, U. Wagner, Z. D. Pešić, T. A. Waigh, and J. M. Rodenburg, Phys. Rev. A **89**(4), 043812 (2014).

[63]L. Peng, J. B. Darren, B. E. Tega, D. P. Aaron, R. Christoph, and M. R. John, J. Opt. **18**(5), 054008 (2016).

[64]M. Guizar-Sicairos, M. Holler, A. Diaz, J. Vila-Comamala, O. Bunk, and A. Menzel, Phys. Rev. B **86**(10), 100103 (2012).

[65]X. Shi, N. Burdet, D. Batey, and I. Robinson, Appl. Sci. **8**(7), 1054 (2018).

[66]M. Newton, Phys. Rev. E **85**(5), 056706 (2012).

[67]X. Huang, R. Harder, G. Xiong, X. Shi, and I. Robinson, Phys. Rev. B **83**(22), 224109 (2011).

[68]M. Newton, R. Harder, X. Huang, G. Xiong, and I. Robinson, Phys. Rev. B **82**(16), 165436 (2010).

[69]X. Shi, J. N. Clark, G. Xiong, X. Huang, R. Harder, and I. K. Robinson, New J. Phys. **15**(12), 123007 (2013).

[70]X. Shi, G. Xiong, X. Huang, R. Harder, and I. Robinson, New J. Phys. **14**, 063029 (2012).

[71]S. J. Leake, M. C. Newton, R. Harder, and I. K. Robinson, Opt. Express **17**(18), 15853–15859 (2009).

[72]N. Burdet, X. Shi, J. N. Clark, X. Huang, R. Harder, and I. Robinson, Phys. Rev. B **96**(1), 014109 (2017).

[73]F. Berenguer de la Cuesta, M. P. Wenger, R. J. Bean, L. Bozec, M. A. Horton, and I. K. Robinson, Proc. Natl. Acad. Sci. U. S. A. **106**(36), 15297–15301 (2009).

[74]F. Berenguer, R. J. Bean, L. Bozec, J. Vila-Comamala, F. Zhang, C. M. Kewish, O. Bunk, J. M. Rodenburg, and I. K. Robinson, Biophys. J. **106**(2), 459–466 (2014).

[75]S. O. Hruszkewycz, Q. Zhang, M. V. Holt, M. J. Highland, P. G. Evans, and P. H. Fuoss, Phys. Rev. A **94**(4), 043803 (2016).

[76]M. V. Holt, S. O. Hruszkewycz, C. E. Murray, J. R. Holt, D. M. Paskiewicz, and P. H. Fuoss, Phys. Rev. Lett. **112**(16), 165502 (2014).

[77]S. O. Hruszkewycz, M. J. Highland, M. V. Holt, D. Kim, C. M. Folkman, C. Thompson, A. Tripathi, G. B. Stephenson, S. Hong, and P. H. Fuoss, Phys. Rev. Lett. **110**(17), 177601 (2013).

[78]S. O. Hruszkewycz, M. V. Holt, C. E. Murray, J. Bruley, J. Holt, A. Tripathi, O. G. Shpyrko, I. McNulty, M. J. Highland, and P. H. Fuoss, Nano Lett. **12**, 5148–5154 (2012).

[79]W. Choi, in *Biomedical Optical Phase Microscopy and Nanoscopy*, edited by N. T. Shaked, Z. Zalevsky, and L. L. Satterwhite (Academic Press, Oxford, 2013), pp. 231–260.

[80]J. M. Blackledge, in *Digital Image Processing*, edited by J. M. Blackledge (Woodhead Publishing, 2005), pp. 273–309.

[81]Y. Cui, Z. Zhong, D. Wang, W. U. Wang, and C. M. Lieber, Nano Lett. **3**(2), 149–152 (2003).

[82]D. Wang, Q. Wang, A. Javey, R. Tu, H. Dai, H. Kim, P. C. McIntyre, T. Krishnamohan, and K. C. Saraswat, Appl. Phys. Lett. **83**(12), 2432–2434 (2003).

[83]E. Garnett and P. Yang, Nano Lett. **10**(3), 1082–1087 (2010).

[84]F. Qian, S. Gradečak, Y. Li, C.-Y. Wen, and C. M. Lieber, Nano Lett. **5**(11), 2287–2291 (2005).

[85]P. Caroff, K. A. Dick, J. Johansson, M. E. Messing, K. Deppert, and L. Samuelson, Nat. Nanotechnol. **4**, 50 (2009).

[86]P. Li, T. Edo, D. Batey, J. Rodenburg, and A. Maiden, Opt. Express **24**(8), 9038–9052 (2016).

[87]M. C. Newton, S. J. Leake, R. Harder, and I. K. Robinson, Nat. Mater. **9**, 120–124 (2010).

[88]D. Dzhigaev, T. Stankevič, Z. Bi, S. Lazarev, M. Rose, A. Shabalin, J. Reinhardt, A. Mikkelsen, L. Samuelson, G. Falkenberg, R. Feidenhans'l, and I. A. Vartanyants, ACS Nano **11**(7), 6605–6611 (2017).

[89]C. Zhu, R. Harder, A. Diaz, V. Komanicky, A. Barbour, R. Xu, X. Huang, Y. Liu, M. S. Pierce, A. Menzel, and H. You, Appl. Phys. Lett. **106**(10), 101604 (2015).

[90]A. Davtyan, V. Favre-Nicolin, R. B. Lewis, H. Küpers, L. Geelhaar, D. Kriegner, D. Bahrami, A. Al-Hassan, G. Chahine, O. Loffeld, and U. Pietsch, MRS Adv. **3**(39), 2317–2322 (2018).

[91]P. Godard, G. Carbone, M. Allain, F. Mastropietro, G. Chen, L. Capello, A. Diaz, T. H. Metzger, J. Stangl, and V. Chamard, Nat. Commun. **2**, 568 (2011).

[92]X. Huang, R. Harder, S. Leake, J. Clark, and I. Robinson, J. Appl. Crystallogr. **45**(Pt 4), 778–784 (2012).

[93]V. Chamard, M. Allain, P. Godard, A. Talneau, G. Patriarche, and M. Burghammer, Sci. Rep. **5**, 9827 (2015).

[94]A. I. Pateras, M. Allain, P. Godard, L. Largeau, G. Patriarche, A. Talneau, K. Pantzas, M. Burghammer, A. A. Minkevich, and V. Chamard, Phys. Rev. B **92**(20), 205305 (2015).

[95]S. O. Hruszkewycz, M. Allain, M. V. Holt, C. E. Murray, J. R. Holt, P. H. Fuoss, and V. Chamard, Nat. Mater. **16**(2), 244–251 (2017).

[96]M. O. Hill, I. Calvo-Almazan, M. Allain, M. V. Holt, A. Ulvestad, J. Treu, G. Koblmüller, C. Huang, X. Huang, H. Yan, E. Nazaretski, Y. S. Chu, G. B. Stephenson, V. Chamard, L. J. Lauhon, and S. O. Hruszkewycz, Nano Lett. **18**(2), 811–819 (2018).

[97]M. Beckers, T. Senkbeil, T. Gorniak, M. Reese, K. Giewekemeyer, S.-C. Gleber, T. Salditt, and A. Rosenhahn, Phys. Rev. Lett. **107**(20), 208101 (2011).

[98]X. Zhu, A. P. Hitchcock, D. A. Bazylinski, P. Denes, J. Joseph, U. Lins, S. Marchesini, H.-W. Shiu, T. Tyliszczak, and D. A. Shapiro, Proc. Natl. Acad. Sci. U. S. A. **113**(51), E8219 (2016).

[99]J. Wu, X. Zhu, M. M. West, T. Tyliszczak, H.-W. Shiu, D. Shapiro, V. Berejnov, D. Susac, J. Stumper, and A. P. Hitchcock, J. Phys. Chem. C **122**(22), 11709–11719 (2018).

[100]Y. Li and W. C. Chueh, Annu. Rev. Mater. Res. **48**(1), 137–165 (2018).

[101]J. Lim, Y. Li, D. H. Alsem, H. So, S. C. Lee, P. Bai, D. A. Cogswell, X. Liu, N. Jin, Y.-s. Yu, N. J. Salmon, D. A. Shapiro, M. Z. Bazant, T. Tyliszczak, and W. C. Chueh, Science **353**(6299), 566 (2016).

[102]M. Lerotic, C. Jacobsen, J. B. Gillow, A. J. Francis, S. Wirick, S. Vogt, and J. Maser, J. Electron Spectrosc. Relat. Phenom. **144–147**, 1137–1143 (2005).

[103]M. Lerotic, C. Jacobsen, T. Schäfer, and S. Vogt, Ultramicroscopy **100**(1), 35–57 (2004).

[104]A. M. Wise, J. N. Weker, S. Kalirai, M. Farmand, D. A. Shapiro, F. Meirer, and B. M. Weckhuysen, ACS Catal. **6**(4), 2178–2181 (2016).

[105]M. Odstrcil, M. Holler, J. Raabe, and M. Guizar-Sicairos, paper presented at the *SPIE Commercial + Scientific Sensing and Imaging*, 2018.

[106]M. Acosta, N. Novak, V. Rojas, S. Patel, R. Vaish, J. Koruza, G. A. Rossetti Jr, and J. Rödel, Appl. Phys. Rev. **4**(4), 041305 (2017).

[107]M. M. Qazilbash, A. Tripathi, A. A. Schafgans, B.-J. Kim, H.-T. Kim, Z. Cai, M. V. Holt, J. M. Maser, F. Keilmann, O. G. Shpyrko, and D. N. Basov, Phys. Rev. B **83**(16), 165108 (2011).

[108]A. Hultgren, M. Tanase, C. S. Chen, G. J. Meyer, and D. H. Reich, J. Appl. Phys. **93**(10), 7554–7556 (2003).

[109]A. Hultgren, M. Tanase, E. J. Felton, K. Bhadriraju, A. K. Salem, C. S. Chen, and D. H. Reich, Biotechnol. Prog. **21**(2), 509–515 (2005).

[110]L. C. C. Arzuza, R. López-Ruiz, D. Salazar-Aravena, M. Knobel, F. Béron, and K. R. Pirota, J. Magn. Magn. Mater. **432**(Supplement C), 309–317 (2017).

[111]J. Dean, M. T. Bryan, T. Schrefl, and D. A. Allwood, J. Appl. Phys. **109**(2), 023915 (2011).

[112]S. Roy, M. Langner, and J. Lee, in *Skyrmions: Topological Structures, Properties, and Applications*, edited by Z. Z. J. Ping Liu and G. Zhao (CRC Press, 2016).

[113]M. C. Langner, S. Roy, S. K. Mishra, J. C. Lee, X. W. Shi, M. A. Hossain, Y. D. Chuang, S. Seki, Y. Tokura, S. D. Kevan, and R. W. Schoenlein, Phys. Rev. Lett. **112**(16), 167202 (2014).

[114]J. C. T. Lee, J. J. Chess, S. A. Montoya, X. Shi, N. Tamura, S. K. Mishra, P. Fischer, B. J. McMorran, S. K. Sinha, E. E. Fullerton, S. D. Kevan, and S. Roy, Appl. Phys. Lett. **109**(2), 022402 (2016).

[115]S. Woo, K. Litzius, B. Krüger, M.-Y. Im, L. Caretta, K. Richter, M. Mann, A. Krone, R. M. Reeve, M. Weigand, P. Agrawal, I. Lemesh, M.-A. Mawass, P. Fischer, M. Kläui, and G. S. D. Beach, Nat. Mater. **15**, 501 (2016).

[116]U. K. Rößler, A. N. Bogdanov, and C. Pfleiderer, Nature **442**, 797 (2006).

[117]A. K. Yadav, C. T. Nelson, S. L. Hsu, Z. Hong, J. D. Clarkson, C. M. Schlepütz, A. R. Damodaran, P. Shafer, E. Arenholz, L. R. Dedon, D. Chen, A. Vishwanath, A. M. Minor, L. Q. Chen, J. F. Scott, L. W. Martin, and R. Ramesh, Nature **530**, 198 (2016).

[118]P. Sutcliffe, Phys. Rev. Lett. **118**(24), 247203 (2017).

[119]J.-S. B. Tai and I. I. Smalyukh, Phys. Rev. Lett. **121**(18), 187201 (2018).

[120]A. Fernández-Pacheco, R. Streubel, O. Fruchart, R. Hertel, P. Fischer, and R. P. Cowburn, Nat. Commun. **8**, 15756 (2017).

[121]R. Ramesh and N. A. Spaldin, Nat. Mater. **6**, 21 (2007).

[122]S.-W. Cheong and M. Mostovoy, Nat. Mater. **6**, 13 (2007).

[123]T. Higuchi, K. Suzumori, and S. Tadokoro, *Next-Generation Actuators Leading Breakthroughs* (Springer International Publishing AG, 2010).

[124]R. Streubel, D. Köhler, R. Schäfer, and L. M. Eng, Phys. Rev. B **87**(5), 054410 (2013).

[125]I. Žutić, J. Fabian, and S. Das Sarma, Rev. Mod. Phys. **76**(2), 323–410 (2004).

[126]S. D. Bader and S. S. P. Parkin, Annu. Rev. Condens. Matter Phys. **1**(1), 71–88 (2010).

[127]Y.-S. Yu, R. Celestre, B. Enders, K. Nowrouzi, H. Padmore, T. Warwick, J.-R. Jeong, and D. A. Shapiro, Microsc. Microanal. **24**(S2), 530–531 (2018).

[128]I. Bykova, K. Keskinbora, U. Sanli, J. Gräfe, M. Bechtel, G. Yu, E. Goering, H. Stoll, G. Schütz, and M. Weigand, Microsc. Microanal. **24**(S2), 34–35 (2018).

[129]C. Donnelly, V. Scagnoli, M. Guizar-Sicairos, M. Holler, F. Wilhelm, F. Guillou, A. Rogalev, C. Detlefs, A. Menzel, J. Raabe, and L. J. Heyderman, Phys. Rev. B **94**(6), 064421 (2016).

[130]A. Tripathi, J. Mohanty, S. H. Dietze, O. G. Shpyrko, E. Shipton, E. E. Fullerton, S. S. Kim, and I. McNulty, Proc. Natl. Acad. Sci. U. S. A. **108**(33), 13393–13398 (2011).

[131]C. Donnelly, M. Guizar-Sicairos, V. Scagnoli, S. Gliga, M. Holler, J. Raabe, and L. J. Heyderman, Nature **547**(7663), 328–331 (2017).

[132]R. Streubel, C.-H. Lambert, N. Kent, P. Ercius, A. T. N'Diaye, C. Ophus, S. Salahuddin, and P. Fischer, Adv. Mater. **30**(27), 1870200 (2018).

[133]R. Streubel, F. Kronast, P. Fischer, D. Parkinson, O. G. Schmidt, and D. Makarov, Nat. Commun. **6**, 7612 (2015).

[134]D. Claire, G. Sebastian, S. Valerio, H. Mirko, R. Jörg, J. H. Laura, and G.-S. Manuel, New J. Phys. **20**(8), 083009 (2018).

[135]D. Lee, R. K. Behera, P. Wu, H. Xu, Y. L. Li, S. B. Sinnott, S. R. Phillpot, L. Q. Chen, and V. Gopalan, Phys. Rev. B **80**(6), 060102 (2009).